Materials Advances

ROYAL SOCIETY OF CHEMISTRY

PAPER

View Article Online
View Journal | View Issue

Check for updates

Cite this: *Mater. Adv.*, 2026, 7, 564

Received 31st July 2025,
Accepted 11th November 2025

DOI: 10.1039/d5ma00827a

rsc.li/materials-advances

Integrated hierarchical Z-scheme BiOCl/NiTiO$_3$ heterostructured photoanode and its photoelectrocatalytic application in ciprofloxacin degradation

Babatope O. Ojo *[a] and Nonhlangabezo Mabuba *[ab]

In this work, we explore the application of a BiOCl/NiTiO$_3$ heterostructured photoanode with a remarkable synergistic advantage and unique band alignment for the photoelectrocatalytic (PEC) degradation of ciprofloxacin. Combining the excellent charge transport of BiOCl and the visible-light absorption of NiTiO$_3$, the BiOCl/NiTiO$_3$ photoanode facilitated electro-hole charge separation and extended light absorption owing to its distinctive band gap energy and visible-light sensitivity. These attributes were confirmed by the impressive charge-transfer advantage (R_{ct} = 157 Ω) and band gap energy (E_g) of 2.08 eV obtained from the Nyquist and Tauc plots of the photoanode. Moreover, the BiOCl/NiTiO$_3$ heterostructured photoanode exhibited a Z-type behaviour, evident by the flow of electrons from the conduction band of BiOCl (with a higher Fermi level) to the valence band of NiTiO$_3$ (with a lower Fermi level). This occurrence made uncombined holes and electrons in the respective valence band of BiOCl and the conduction band of NiTiO$_3$ readily available for the generation of reactive oxygen species in the system. The BiOCl/NiTiO$_3$ heterostructure architecture significantly aided the photoelectrocatalytic degradation of ciprofloxacin in water, achieving a remarkable 94% degradation efficiency. In addition, the heterostructured photoanode displayed outstanding stability and reusability, making it a distinct advanced material for real-time operations. Furthermore, the findings from this work demonstrate a reliable strategy for high-performance PEC design while contributing to a sustainable approach for wastewater remediation applications.

1. Introduction

Growing concerns over the health and economic impacts of environmental pollution driven by increasing levels of organic pollutants in waterbodies have intensified over the last decade.[1–3] This is particularly so because research breakthroughs in the pharmaceutical industry geared toward combating various health challenges have resulted in unprecedented demand for various pharmaceutical products. Among commonly detected classes of pharmaceutical pollutants in wastewater, antibiotics remain a prevalent member often reported.[4,5] Since most of these products are organic, a burgeoning level of these products has reportedly been detected in waterbodies across the globe.[6] An unsettling risk of developing antibiotic-resistant pathogens may occur from long-term consumption of water polluted with antibiotics.[7,8] With increasing pressure on the supply of clean, potable water to various classes of society, the capacity of many conventional water purification systems has become limited.[9] The threat posed by this limitation has spurred a significant quest for robust, easily accessible and cost-effective approaches towards achieving water availability across the globe.

The application of advanced materials for effective wastewater remediation has culminated in the development of research on advanced oxidation processes, particularly photoelectrocatalysis (PEC).[10–12] PEC involves converting photon energy into chemical energy through photogenerated charge carriers, produced by the interaction of visible light with semiconductors. Consequently, the generated chemical energy is crucial for producing reactive species capable of degrading the organic bonds of molecules non-selectively. Interestingly, photoanode heterostructures combining two or more semiconductors with complementary properties have emerged as promising advanced materials for effective remediation of organic pollutants in wastewater. Owing to their charge-separation advantage and superior light-absorption properties, heterostructure photoanodes have effectively addressed the challenge

---

[a] Department of Chemical Sciences, University of Johannesburg, South Africa. E-mail: ojobabatope86.bo@gmail.com, nmabuba@uj.ac.za
[b] Centre for Nanomaterials Science Research, University of Johannesburg, South Africa

of instability and rapid charge carrier recombination often associated with PEC.[13,14] Among the numerous candidates for heterostructured photoanodes, bismuth oxychloride (BiOCl) semiconductor has garnered tremendous attention due to its distinctive photocatalytic attributes.[15–17] Peculiarly, a unique bandgap range, specialized layered structure, highly reactive surface area and notable stability possessed by BiOCl favour its applications in energy and storage devices, water remediation, water splitting, and hydrogen generation. However, rapid recombination of generated charge-carrier species often impedes their photocatalytic application.[18–20]

Recently, nickel titanate ($NiTiO_3$), a perovskite oxide distinct for its narrow band gap energy, excellent stability, structural robustness and scalable industrial applications, has positioned it as a complementary semiconductor for heterostructured design.[21–23] These attributes confer excellent photocatalytic activity on $NiTiO_3$-based heterojunctions, thereby promoting charge separation through interfacial electron transfer and remarkable band alignment for PEC applications.[22] Harmonizing the intrinsic properties of BiOCl and $NiTiO_3$ during heterostructured photoanode design can facilitate easy and quick reactive oxygen species (ROS) generation in photoelectrocatalysis. Moreover, a narrowed band gap often observed in heterostructured photoanodes can promote extended light absorption by reducing photocorrosion and improving stability and reusability of the photoanode over multiple cycles.

PEC applications in wastewater remediation continue to thrive as a reliable approach for recalcitrant organic pollutant mineralization in water. PEC involves the synergistic combination of photocatalytic and electrocatalytic principles to enhance ROS generation and improve charge carrier separation in water treatment applications.[13,24] Applying renewable solar energy and lower bias potential than that required in electrocatalysis due to photo-activity input has broadened the scope of PEC over the years. This stems from the ease of electron flow across the electrolyte-semiconductor interface occasioned by contact initiation between the semiconductor and the electrolyte. A band bending known as a built-in electric field often ensues, creating an equilibrium potential within the system.[25] This event usually enhances light absorption and charge-carrier separation at the interface of a heterostructured semiconductor. Additionally, owing to its cost-effectiveness, accessibility to photoactive advanced materials, and the application of doped and heterostructured photoanode designs, visible-light spectrum absorption has become easily attainable in PEC reactions. These advantages have also been explored for hybrid technologies, including photo-electro-Fenton,[26] sono-photoelectrocatalysis[27] and photo-electrocoagulation[28–30] in wastewater treatment processes. Ultimately, photogenerated holes (h^+) and electrons (e^-), as well as directly or indirectly generated oxidative species such as hydroxyl radical ($^\bullet OH$), superoxide radical ($O_2^{\bullet -}$), enjoy extended lifespans, thus amplifying the reaction kinetics of the process.

This study explores the application of a novel BiOCl/$NiTiO_3$ heterostructured photoanode for the degradation of ciprofloxacin, a recalcitrant antibiotic commonly detected in wastewater under photoelectrocatalytic conditions. Physicochemical and electrochemical characterization were conducted to investigate the structural, morphological and electrochemical properties of the designed photoanode. Also, the synergistic advantage of combining photocatalysis and electrocatalysis in PEC was examined through reaction kinetics. The reusability and the identification of the reactive species generated in the PEC system were equally investigated. Finally, a suitable reaction scheme for the heterostructured photoanode was examined based on its electrochemical properties.

2. Materials and methods

2.1 Chemical

Reagents used in this study were sourced from Merck (South Africa) and employed for various applications without further purification. Bismuth nitrate pentahydrate ($Bi(NO_3)_3\cdot 5H_2O$), sodium chloride (NaCl), nickel acetate tetrahydrate ($Ni(CH_3COO)_2\cdot 4H_2O$) and titanium butoxide ($(C_4H_9O)_4Ti$) were the starting materials used in synthesizing BiOCl and $NiTiO_3$ semiconductors. Acetic acid (CH_3COOH), ethanol (C_2H_5OH) and ethylene glycol were used as solvents during the synthetic process. Fluorine-doped tin oxide (FTO) glass ($L \times W \times D$: 50 mm × 15 mm × 2.2 mm, surface resistivity of $\sim 13\ \Omega\ sq^{-1}$) was used as the substrate upon which the BiOCl/$NiTiO_3$ heterostructured photoanode was immobilized. Polyvinylidene fluoride (PVDF) and *N*-methyl-2-pyrrolidone (NMP) were used as binding agents to immobilize the photoanode on the FTO glass. The scavenging of reactive species during the PEC experiments was carried out in the presence of terephthalic acid (TA, 1 mmol L^{-1}), *p*-benzoquinone (BQ, 1 mmol L^{-1}), ethylenediaminetetraacetic acid (EDTA, 1 mmol L^{-1}) and silver nitrate ($AgNO_3$, 1 mmol L^{-1}) as the scavenging agents for trapping hydroxyl radicals ($^\bullet OH$) and superoxide radicals ($O_2^{\bullet -}$, holes (h^+) and electrons (e^-), respectively.

2.2 Synthesis of BiOCl

BiOCl was synthesized using the hydrothermal method. Firstly, 0.015 mmol of $Bi(NO_3)_3\cdot 5H_2O$ was dispersed in 20 mL of ethylene glycol. The mixture was stirred on a magnetic stirrer at room temperature for 30 min before adding 0.01 mmol of NaCl. The mixture was further stirred for 2 h until a homogeneous mixture was obtained. The mixture was later transferred into a Teflon-lined autoclave and heated at 180 °C for 12 h. Upon cooling, the resulting product was washed several times with deionized water and ethanol. Subsequently, the product was dried at 60 °C for 12 h to obtain the BiOCl powder.

2.3 Synthesis of $NiTiO_3$

$NiTiO_3$ was synthesized using a solvothermal method. Briefly, a 1 : 1 mole composition comprising $Ni(CH_3CO_2)_2\cdot 4H_2O$ (0.05 mmol) and $Ti(C_4H_9O)_4$ (0.05 mmol) was dispersed in a mixture of ethanol and acetic acid. The mixture was stirred at room temperature for 2 h until a viscous sol–gel was obtained. The obtained sol–gel was dried for 24 h at 80 °C. The obtained $NiTiO_3$ was further subjected to hydrothermal treatment by dispersing it into 3 M KOH and transferring the mixture into a Teflon-lined autoclave. The autoclave containing the mixture was then heated for 24 h at 160 °C. Upon cooling to room temperature, the $NiTiO_3$ was washed several times with deionized water and ethanol to remove residual carbonate and other dissolved impurities. Finally, the pure $NiTiO_3$ was dried at 60 °C for 12 h to obtain $NiTiO_3$ powder.

2.4 Synthesis of the BiOCl/$NiTiO_3$ heterostructured photocatalyst

The BiOCl/$NiTiO_3$ heterostructured photocatalyst was prepared by stirring 50 wt% of BiOCl and 50 wt% of $NiTiO_3$ in ethanol for 10 min. The composite was oven-dried at 120 °C for 3 h to obtain the BiOCl/$NiTiO_3$ powder.

2.5 Characterization of photocatalysts

X-ray diffractometer (Rigaku Ultima IV, Japan) using Cu Kα radiation (k = 0.15406), coupled with a K-beta filter at 30 mA and 40 kV, was employed to study the purity and degree of crystallinity of the prepared BiOCl, $NiTiO_3$, and BiOCl/$NiTiO_3$ powders. X-ray photoelectron spectroscopy (Thermo, ESCAlab 250Xi, USA) was used to analyze the chemical and electronic state of the atoms in the photocatalysts. Scanning electron microscopy (SEM) (Zeiss 540 ultra, Germany), attached to an energy-dispersive X-ray spectrometer (EDS), was employed to study the morphology, elemental composition and elemental mapping of the materials. The optical property of the semiconductors was measured using UV-vis diffuse reflectance spectroscopy.

2.6 Fabrication of the BiOCl/$NiTiO_3$ heterostructured photoanode

The BiOCl/$NiTiO_3$ heterostructured photoanode was fabricated by drop-casting a BiOCl/$NiTiO_3$ slurry on a pre-treated FTO glass. The BiOCl/$NiTiO_3$ slurry was prepared by mixing 50 mg of the BiOCl/$NiTiO_3$ powder in 50 wt% NMP and 5 wt% of PVDF. This was followed by careful coating of the BiOCl/$NiTiO_3$ slurry onto the conductive surface of the FTO glass to obtain a uniformly distributed BiOCl/$NiTiO_3$ film on the substrate. The electrode (geometrical area: 2 cm^{-2}) was then left to dry in an oven at 60 °C for 2 h. The same method was employed in preparing the respective BiOCl and $NiTiO_3$ photoanodes.

2.7 Electrochemical and photoelectrochemical characterization of the photoanode

Electrochemical properties of the photoanodes were investigated using an Autolab potentiostat/galvanostat (PGSTAT204, Netherlands). The prepared photoanodes were connected to the potentiostat as working electrodes, while a platinum wire and an Ag/AgCl electrode were connected as the respective counter and reference electrodes. Electrochemical impedance spectroscopy (EIS) and Mott Schottky analysis were performed in 5 mM ferri/ferrocyanide solution $[Fe(CN)_6]^{3-/4-}$ at a scan rate of 20 mV s^{-1}, frequency range of 100 kHz to 0.1 Hz, and bias potential of 0.22 V. Linear sweep voltammetry (LSV) was used to obtain the onset potential of the photoanodes, and chronoamperometry measurement was used to investigate the photocurrent density response of the photoanodes. These analyses were conducted in 0.1 M Na_2SO_4 at neutral pH, in the presence of a 150 W LED lamp as the light source. All characterizations were carried out at neutral pH.

2.8 Photoelectrocatalytic degradation experiment

PEC and electrocatalytic (EC) experiments were conducted using a power source for bias current supply to the system. A 150 W LED lamp was used as the light source for photocatalytic (PC) and PEC experiments. During the PEC degradation experiment, the prepared photoanode and a platinum wire were connected to the power source as anode and cathode, respectively. The PEC reaction was performed in 50 mL of 5 mg L^{-1} ciprofloxacin (CPX) concentration with 0.1 M Na_2SO_4 as the supporting electrolyte at a known applied current density. For the EC degradation experiment, the same CPX concentration was subjected to the same operating conditions as the PEC technique, but without a light source. During the PC degradation experiment, the photoanode was exposed to the light source without applying a current density. This was equally performed using the same volume and concentration of CPX. The influence of various applied current densities and different initial concentrations of CPX on the performance of the heterostructured photoanode was also examined. Aliquots of CPX solution were collected from the reactor at time intervals of 20 min for 120 min to analyze the decay patterns during PEC, EC and PC. A UV-visible spectrophotometer was used to investigate the downward trend of CPX concentration during the experiments. The degradation efficiency of CPX was obtained using the formula in eqn (1).

$$\text{Degradation efficiency (\%)} = \frac{c_0 - c_t}{c_0} \times 100\% \qquad (1)$$

Here, c_0 and c_t are the initial and final concentrations, respectively.

3. Results and discussions

3.1 Structural and morphological properties of the photocatalysts

The X-ray diffraction (XRD) analysis was conducted to identify the crystal structure and confirm the synthesis of the photocatalysts (Fig. 1a). The XRD pattern of $NiTiO_3$ shows a strong similarity with its hexagonal phase (JCPDS card no. 017–0617), with notable peaks observed at $2\theta \approx 24°$, 32.8°, 35.5°, 40.8°, 49.3°, 53.8°, and the twin peaks at 62.2° 63.8°. The observed peaks are indexed as diffraction planes (012), (104), (110), (113), (024), (116), (214), and (300), respectively.[31] Similarly, the XRD pattern of BiOCl corresponds strongly to its tetragonal phase (JCPDS card no. 01-0600). Major peaks observed for BiOCl at $2\theta \approx 11.6°$, 24.1°, 25.2°, 33.3°, and 36.4° correspond to the (001), (011), (110), (102), and (003) diffraction planes, respectively.[32] The outlined peaks were observed on the XRD pattern of BiOCl/$NiTiO_3$, demonstrating that the heterostructured photocatalyst was satisfactorily formed. However, the weak diffraction peaks of $NiTiO_3$ observed on the XRD graph of BiOCl/$NiTiO_3$ signify a better dispersion of BiOCl on the $NiTiO_3$.

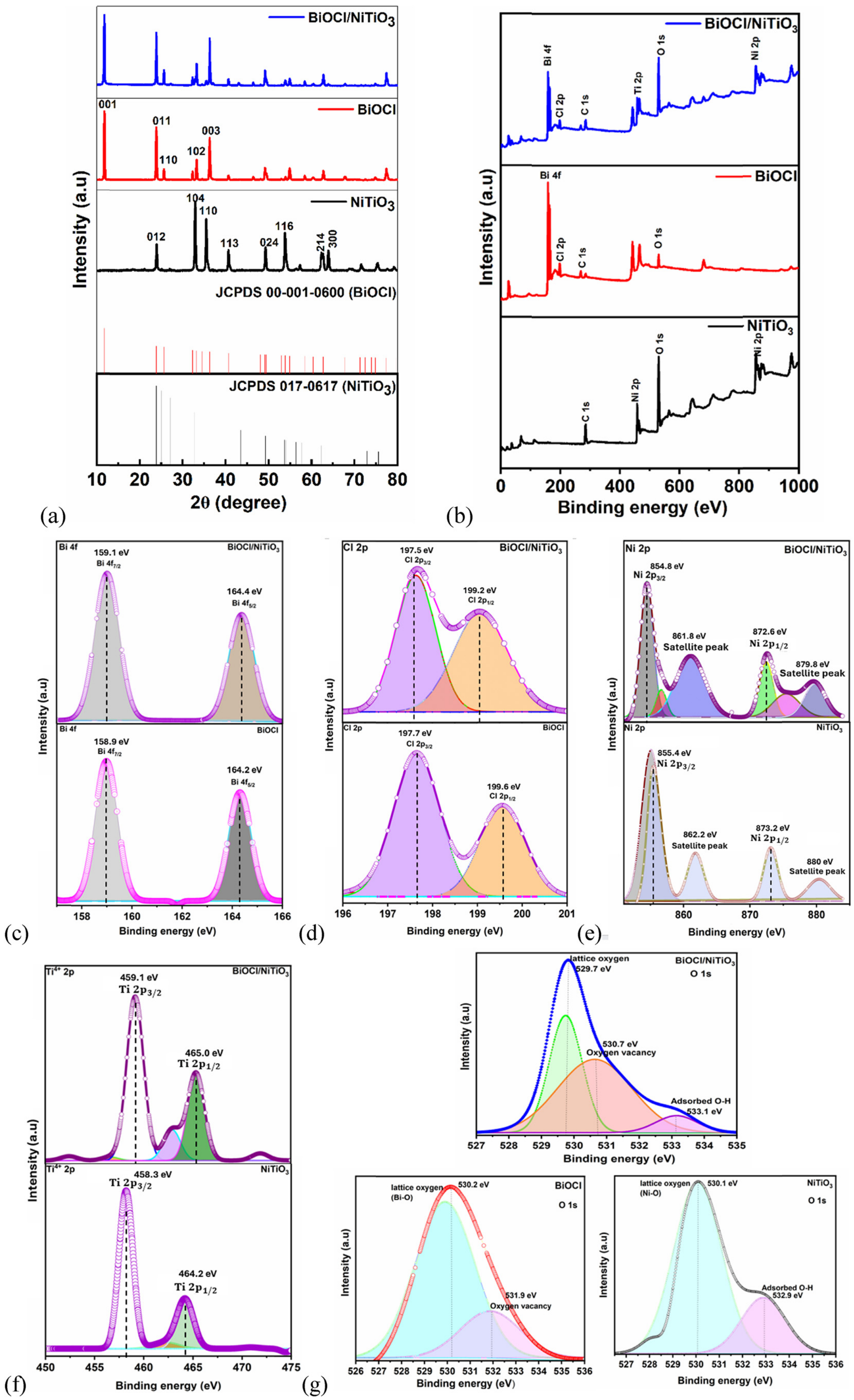
BiOCl/NiTiO3
001
011
110
102
003
BiOCl
104
110
012
113
024
116
214
300
NiTiO3
JCPDS 00-001-0600 (BiOCl)
JCPDS 017-0617 (NiTiO3)
Intensity (a.u)
10 20 30 40 50 60 70 80
2θ (degree)
(a)
BiOCl/NiTiO3
Bi 4f
Cl 2p
C 1s
Ti 2p
O 1s
Ni 2p
BiOCl
Bi 4f
Cl 2p
C 1s
O 1s
NiTiO3
C 1s
Ni 2p
O 1s
Ni 2p
Intensity (a.u)
0 200 400 600 800 1000
Binding energy (eV)
(b)
Bi 4f BiOCl/NiTiO3
159.1 eV Bi 4f7/2
164.4 eV Bi 4f5/2
Bi 4f BiOCl
158.9 eV Bi 4f7/2
164.2 eV Bi 4f5/2
Intensity (a.u)
158 160 162 164 166
Binding energy (eV)
(c)
Cl 2p BiOCl/NiTiO3
197.5 eV Cl 2p3/2
199.2 eV Cl 2p1/2
Cl 2p BiOCl
197.7 eV Cl 2p3/2
199.6 eV Cl 2p1/2
Intensity (a.u)
196 197 198 199 200 201
Binding energy (eV)
(d)
Ni 2p BiOCl/NiTiO3
854.8 eV Ni 2p3/2
861.8 eV Satellite peak
872.6 eV Ni 2p1/2
879.8 eV Satellite peak
Ni 2p NiTiO3
855.4 eV Ni 2p3/2
862.2 eV Satellite peak
873.2 eV Ni 2p1/2
880 eV Satellite peak
Intensity (a.u)
860 870 880
Binding energy (eV)
(e)
Ti4+ 2p BiOCl/NiTiO3
459.1 eV Ti 2p3/2
465.0 eV Ti 2p1/2
Ti4+ 2p NiTiO3
458.3 eV Ti 2p3/2
464.2 eV Ti 2p1/2
Intensity (a.u)
450 455 460 465 470 475
Binding energy (eV)
(f)
lattice oxygen 529.7 eV
BiOCl/NiTiO3 O 1s
530.7 eV Oxygen vacancy
Adsorbed O-H 533.1 eV
Intensity (a.u)
527 528 529 530 531 532 533 534 535
Binding energy (eV)
lattice oxygen (Bi-O) 530.2 eV
BiOCl O 1s
531.9 eV Oxygen vacancy
Intensity (a.u)
526 527 528 529 530 531 532 533 534 535 536
Binding energy (eV)
lattice oxygen (Ni-O) 530.1 eV
NiTiO3 O 1s
Adsorbed O-H 532.9 eV
Intensity (a.u)
527 528 529 530 531 532 533 534 535 536
Binding energy (eV)
(g)

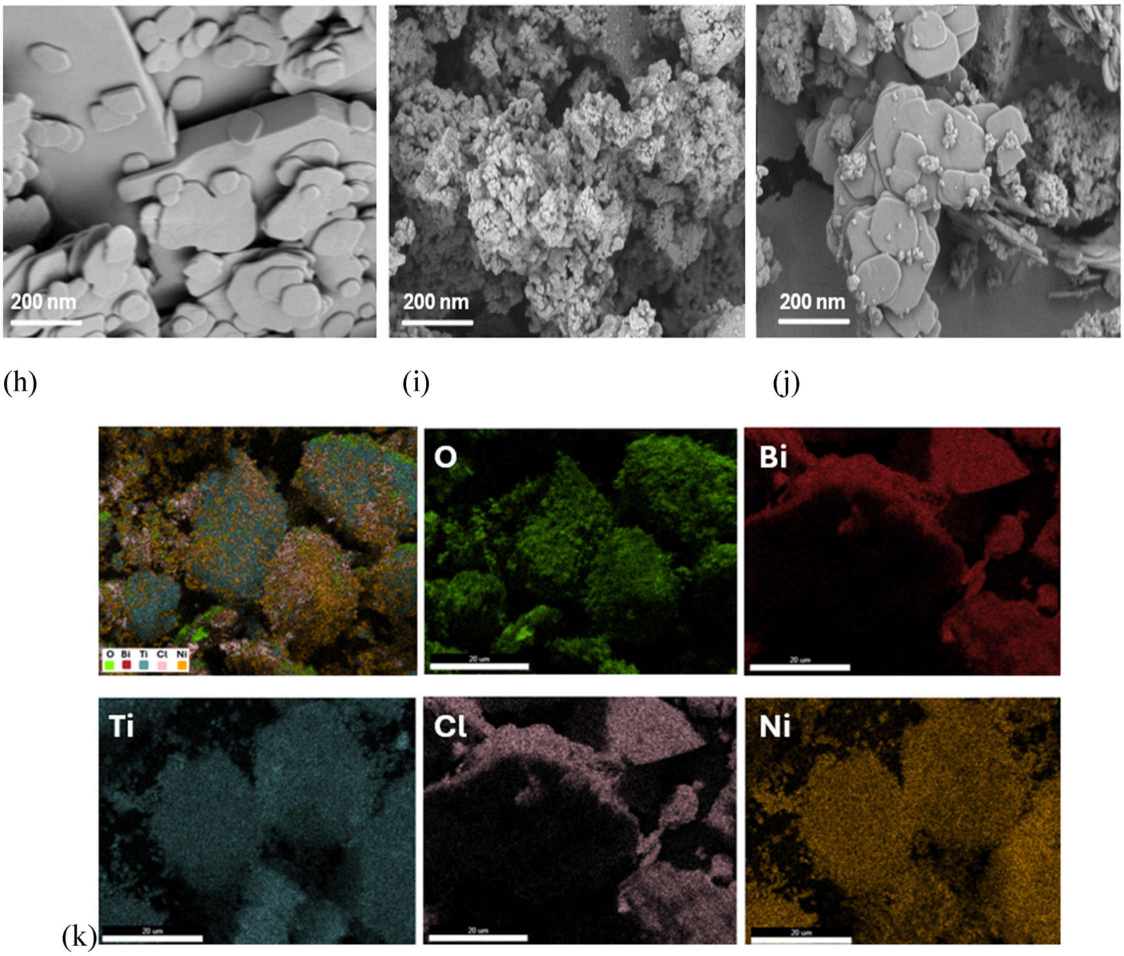

Fig. 1 (a) XRD patterns of $NiTiO_3$, BiOCl and BiOCl/$NiTiO_3$ semiconductors, (b) XPS survey profile of $NiTiO_3$, BiOCl and BiOCl/$NiTiO_3$ semiconductors. High resolution XPS spectra of (c) Bi 4f, (d) Cl 2p, (e) Ni 2p, (f) Ti 2p, and (g) O 1s of $NiTiO_3$, BiOCl, and BiOCl/$NiTiO_3$ semiconductors. SEM images of (h) BiOCl, (i) $NiTiO_3$, (j) BiOCl/$NiTiO_3$ semiconductors. (k) Elemental mapping of the BiOCl/$NiTiO_3$ heterostructured semiconductor.

X-ray photoelectron spectroscopy (XPS) analysis was also conducted to investigate the chemical composition and electronic states of the photocatalysts. The survey scans of BiOCl, $NiTiO_3$, and BiOCl/$NiTiO_3$ photocatalysts are presented in Fig. 1b, indicating the presence of bismuth (Bi), nickel (Ni), titanium (Ti), chlorine (Cl), and oxygen (O), along with their corresponding peaks. The deconvoluted spectra of the Bi $4f_{7/2}$ electronic state reveal a shift in the binding energy from 158.9 eV to 159.1 eV in BiOCl and the heterostructured BiOCl/$NiTiO_3$, respectively (Fig. 1c). A comparable shift was also observed from 164.2 eV to 164.4 eV for the electronic state of Bi $4f_{5/2}$ as the BiOCl/$NiTiO_3$ heterostructure photoanode was formed. The presence of Bi $4f_{7/2}$ and Bi $4f_{5/2}$ peaks demonstrates the existence of the Bi^{3+} oxidation state in pristine BiOCl[33,34] and BiOCl/$NiTiO_3$ heterostructured semiconductor. The deconvoluted spectra of the Cl 2p valence state (Fig. 1d) equally reveal a shift in the binding energy from 197.7 eV to 197.5 eV (Cl $2p_{3/2}$) and 199.6 eV to 199.2 eV (Cl $2p_{1/2}$) upon the formation of the BiOCl/$NiTiO_3$ heterostructured photoanode. These observed shifts in binding energies can be attributed to electron redistribution within the BiOCl/$NiTiO_3$ heterostructured photoanode crystal structure, a vital development for charge separation. The shifts also demonstrate electron density variation across the BiOCl/$NiTiO_3$ interface, facilitating photogenerated charge separation through charge localization in distinctive sites.[35] Moreover, the $[Bi_2O_2]^{2+}$ and Cl^- layered structure formed in BiOCl can promote charge transportation and light absorption extension in the BiOCl/$NiTiO_3$ photoanode through internal electric field generation. Similarly, a backward shift in binding energies was observed from 855.4 eV to 854.8 eV and 873.2 eV to 872.6 eV in the respective Ni $2p_{3/2}$ and Ni $2p_{3/2}$ electronic states (Fig. 1e), further establishing the formation of the heterostructured photoanode. The two satellite peaks at 862.2 eV and 880 eV demonstrate the presence of Ni^{2+} oxidation state in $NiTiO_3$.[21,36] These peaks were also observed at 861.8 eV and 879.8 eV, further confirming the interfacial interaction between BiOCl and $NITiO_3$ semiconductors. The presence of Ti $2p_{3/2}$ and Ti $2p_{1/2}$ peaks (Fig. 1f) demonstrates the existence of the Ti^{4+} oxidation state in pristine $NiTiO_3$.[37] Ti $2p_{3/2}$ and Ti $2p_{1/2}$ electronic states also displayed notable shifts from 458.3 eV to 459.1 eV and 464.2 eV to 465 eV, respectively, as the BiOCl/$NiTiO_3$ heterostructured photocatalyst was formed.

The O 1s peaks observed at 530.2 eV and 531.9 eV correspond to the Bi–O bond and oxygen vacancy in BiOCl,[38,39] while $NiTiO_3$ peaks at 530.1 eV and 532.9 eV correspond to Ni–O bond and physically adsorbed oxygen[40] (Fig. 1g). The lattice oxygen Bi–O of BiOCl at 530.2 eV and $NiTiO_3$ lattice oxygen Ni–O at 530.1 eV were observed to have shifted to a lower binding energy at 529.7 eV for BiOCl/$NiTiO_3$. Similarly, the oxygen vacancy possessed by BiOCl at 531.9 eV was also observed to have shifted to a lower binding energy at 530.7 eV in the BiOCl/$NiTiO_3$ semiconductor. This red shift is indicative of electron transfer at the interface of the BiOCl/$NiTiO_3$ heterostructure semiconductor. Notably, the area covered by the oxygen vacancy in the BiOCl/$NiTiO_3$ heterostructured semiconductor is significantly wider than that of pristine BiOCl. This suggests that surface modification caused by the presence of oxygen vacancies in BiOCl/$NiTiO_3$ can enhance charge separation and water dissociation remarkably, resulting in abundant surface hydroxyl groups needed for the degradation process.[35] In addition, red shifts observed in Cl 2p, Ni 2p and O 1s valence states suggest the occurrence of electron redistribution in the BiOCl/$NiTiO_3$ semiconductor. Moreover, blue shifts observed in the Bi 4f and Ti 2p spectra can be attributed to an increase in electron density as the interfacial and ionic interactions between BiOCl and $NiTiO_3$ were established.

The surface morphology of the pristine and heterostructure semiconductors was determined using scanning electron microscopy (SEM). BiOCl displayed irregular, interconnected, dispersed, and layered plate-like microspheres (Fig. 1h). With slight roughness on the boundaries of the particles, the linkage between the BiOCl particles allows for a suitable deposition and lacing of the other material on their surface. However, $NiTiO_3$ exhibits a blend of grains with uneven sizes (Fig. 1i). The interactions linking these grains led to the formation of pores of varying sizes. Notably, the composition of these particles shows random dispersal of $NiTiO_3$ particles on the BiOCl plate-like particles (Fig. 1j). The coalescence observed with the BiOCl/$NiTiO_3$ heterostructured photocatalyst shows a healthy interaction between both pristine materials, suitable for light absorption in the heterostructure. The interfacial properties displayed by the heterostructure indicate that the BiOCl/$NiTiO_3$ semiconductor was successfully synthesized. The EDX spectrum of the BiOCl/$NiTiO_3$ heterostructured semiconductor shown in Fig. S1 reveals the presence of Bi, Ni, Ti, O, and Cl in the composite. The uniform distribution of atoms in the composite is shown in the EDX mapping (Fig. 1k), further establishing a successful synthesis of the heterostructure.

3.2 Electrochemical and photoelectrochemical properties of the photoanodes

Electrochemical impedance spectroscopy (EIS) was conducted to investigate the charge transport efficiency of the photoanodes. Fig. 2a presents the Nyquist plot of the fabricated photoanodes, with charge transfer resistances (R_{ct}) of 392, 230, and 157 Ω associated with $NiTiO_3$, BiOCl, and BiOCl/$NiTiO_3$ photoanodes, respectively. Notably, a smaller impedance arc in the Nyquist plot corresponds to improved charge transfer efficiency.[41] These results demonstrate that the BiOCl/$NiTiO_3$ heterostructured photoanode displays a more desirable charge transfer efficiency than the individual BiOCl and $NiTiO_3$ photoanodes. This indicates an enhanced charge transport mechanism in the BiOCl/$NiTiO_3$ photoanode, boosting its conductivity and promoting the migration efficiency of photogenerated charge carriers. Moreover, a harmonious interfacial interaction developed between BiOCl and $NiTiO_3$ photoanodes gave rise to band alignment in the BiOCl/$NiTiO_3$ heterostructured photocatalyst. This interaction can propel charge separation in the semiconductor, improving the availability of charged species and reducing the difficulty of charge transfer in the system.

Linear sweep voltammetry (LSV) was employed to investigate the onset potential and current density of the photoanodes at neutral pH. As presented in Fig. 2b, an onset potential of 1.39 V was obtained for the BiOCl/$NiTiO_3$ heterostructured photoanode as compared to a delayed potential of 1.53 V and 1.57 V for BiOCl and $NiTiO_3$ photoanodes, respectively. Since the obtained values exceed the minimum potential of 1.23 V *vs.* RHE required for the oxygen evolution reaction (OER) in water splitting,[42,43] the BiOCl/$NiTiO_3$ heterostructured photoanode represents a conservative potential demand for oxidation reactions compared with other pure semiconductors. Furthermore, the highest current density of 14.93 mA cm^{-2} for the BiOCl/$NiTiO_3$ photoanode exceeds 2.5 times the obtained current densities for BiOCl and $NiTiO_3$ photoanodes, suggesting that the ease of ROS generation favours the BiOCl/$NiTiO_3$ heterostructured photoanode over the individual photoanodes. This validates the charge mobility strength inherent in the BiOCl/$NiTiO_3$ heterojunction photoanode over the pristine semiconductors, as confirmed by the EIS results.

The transient photocurrent density was also investigated to assess the photogenerated charge separation capability of the photoanode at neutral pH. An impressive photocurrent density of 5.36 μA cm^{-2} was obtained for the BiOCl/$NiTiO_3$ heterostructured photoanode compared to 2.77 μA cm^{-2} and 2.62 μA cm^{-2} for BiOCl and $NiTiO_3$ photoanodes, respectively (Fig. 2c). This reveals that a significant suppression of photogenerated charge carrier (hole–electron) recombination was better achieved in the BiOCl/$NiTiO_3$ heterostructured photoanode over the individual photoanodes. A linear correlation validating a mutual relationship between the transient photocurrent of semiconductors and photogenerated charge separation has been previously established.[44] Consequently, improved light absorption efficiency and reduced photocorrosion phenomenon arising from improved interfacial charge transfer will be more prevalent in the BiOCl/$NiTiO_3$ heterostructured photoanode than in the pristine photoanodes. Additionally, band alignment arising from the favourable interfacial properties of the heterostructure can lower charge recombination, thus improving the photocurrent response of the semiconductor.

3.3 Optical properties of the photocatalysts

The optical properties of the semiconductors were analyzed to determine their light absorption regions and band gap energies. As presented in Fig. 2d, $NiTiO_3$ and BiOCl displayed a strong absorption edge around 460 nm and 395 nm, respectively.

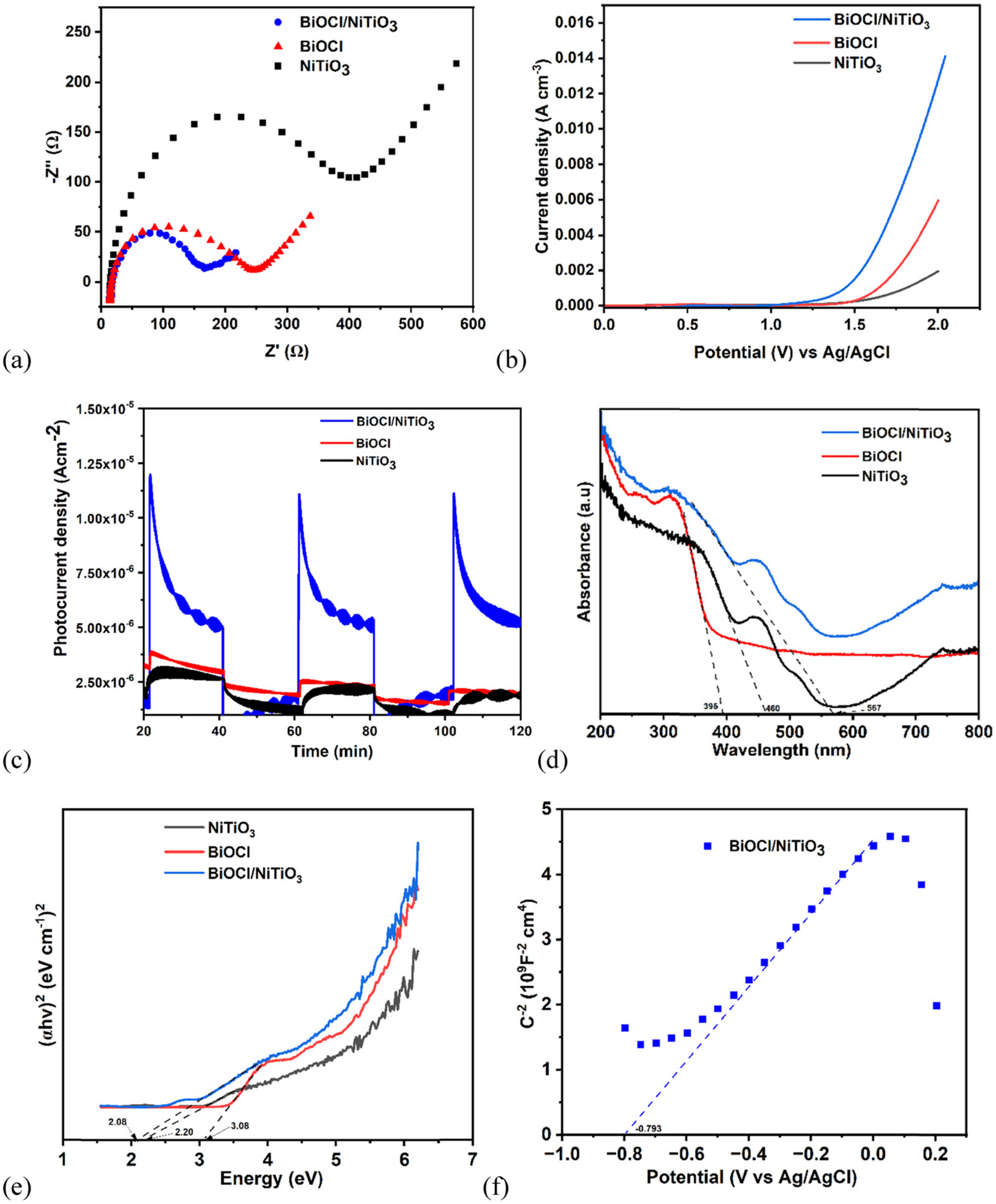

Fig. 2 (a) Nyquist plot of the photoanodes obtained in 5 mM $[Fe(CN)_6]^{3-/4-}$ containing 0.1 M KCl, in frequency range of 100 kHz to 0.1 Hz, (b) linear sweep voltammograms of the photoanodes in 0.1 M Na_2SO_4 at a scan rate of 50 mV, (c) transient photocurrent density of the photoanodes in 0.1 M Na_2SO_4, (d) UV-vis DRS spectra of $NiTiO_3$, BiOCl and BiOCl/$NiTiO_3$, (e) Tauc plots of the photoanodes, and (f) Mott Schottky plot of the BiOCl/$NiTiO_3$ heterostructured photoanode.

Harmoniously, the BiOCl/$NiTiO_3$ photocatalyst equally displayed strong absorption in the visible light region with an absorption edge at 567 nm. The shift of the BiOCl/$NiTiO_3$ absorption edge to a more visible-light region indicates a broadened light absorption capacity, arising from the conducive interfacial synergy between BiOCl and $NiTiO_3$ photocatalysts.

Moreover, the band gap energies of the photocatalysts were obtained from UV-vis diffuse reflectance spectroscopy data fitted to the Tauc equation (eqn (2)).

$$\alpha hv = \beta(hv - E_g)^{n/2} \tag{2}$$

where α, h, v, and β represent the absorption coefficient, Planck's constant, incident light or photon frequency, and proportionality constant, respectively. Moreover, n is a constant that depends solely on the optical transition characteristics of the semiconductors under consideration, and E_g is the band gap energy. For a direct allowed transition in semiconductors, $n = 1/2$ and $n = 2$ for an indirect allowed transition. Based on the direct allowed transition, the band gap energy of the semiconductors was obtained from the plot of $(\alpha hv)^2$ against hv. As presented in Fig. 2e, BiOCl, $NiTiO_3$, and BiOCl/$NiTiO_3$ semiconductors conformed to a direct allowed transition with band gap energies of 3.08 eV, 2.20 eV, and 2.08 eV, respectively. A narrower bandgap observed for the heterojunction formed by BiOCl and $NiTiO_3$ demonstrates the successful design of a viable visible light-harvesting photoanode. The conduction and valence bands of BiOCl and $NiTiO_3$ were obtained from eqn (3) and (4).

$$E_{CB} = X - E_c - 0.5E_g \tag{3}$$

$$E_{VB} = E_{CB} + E_g \tag{4}$$

From these equations, E_{CB}, E_{VB}, and E_C represent the conduction band edge potential, valence band edge potential, and free electron energy on the hydrogen scale, often approximated to be 4.50 eV, respectively. Moreover, X is the electronegativity of the semiconductor, usually obtained as the geometrical mean value of the absolute electronegativity of the atomic constituents of a semiconductor. The calculated X values of BiOCl and $NiTiO_3$ are 6.37 eV and 5.79 eV, respectively, and E_g is the band gap energy of the semiconductor. Thus, 0.32 eV and 3.40 eV are the respective E_{CB} and E_{VB} values obtained for BiOCl, while −0.74 eV and 1.46 eV are the respective E_{CB} and E_{VB} values obtained for $NiTiO_3$.

The Mott Schottky analysis was performed to determine the flat band potential and charge carrier density of the photoanodes. Using the Mott Schottky equation (eqn (5)), the Mott Schottky plots for each photoanode were obtained from the graph of $1/c^2$ *versus* potential (eV *vs.* Ag/AgCl).

$$\frac{1}{c^2} = \left(\frac{2}{\varepsilon\varepsilon_0 e N_D}\right)\left(E_{app} - E_{fb} - \frac{k_B T}{e}\right) \tag{5}$$

Here, c, ε, ε_0, e, N_D, E_{app}, E_{fb}, k_B, T are the capacitance at the electrolyte/semiconductor interface (F cm^{-2}), dielectric constant of the semiconductor, vacuum permittivity (8.85×10^{-14} F cm^{-1}), elementary charge (1.6×10^{-19} C), donor density (n-type semiconductor) or acceptor density (p-type semiconductor), applied potential (V), flat band potential (V), Boltzmann constant and absolute temperature (278 K), respectively.

The flat band potential was obtained as the X-intercept after extrapolating the linear fit of the plot. BiOCl has a negative slope (Fig. S2), indicative of a p-type behaviour, while $NiTiO_3$ has a positive slope (Fig. S3), indicative of n-type semiconductors. Flat band potentials of 0.17 V, −0.55 V, and −0.79 V (*vs.* Ag/AgCl) were obtained for BiOCl, $NiTiO_3$, and BiOCl/$NiTiO_3$ photoanodes, respectively. Using the formula in eqn (6), the flat band potential *vs.* normal hydrogen electrode (NHE) values of the photoanodes were estimated as 0.37 eV and −0.36 eV for BiOCl and $NiTiO_3$ photoanodes. These results are a product of electrolyte–semiconductor interfacial interactions, electrode geometry, electrode surface area, and smoothness of the electrode surface.[45] Moreover, the negative shift obtained for the BiOCl/$NiTiO_3$ photoanodes at −0.59 eV *vs.* NHE, as against −0.16 eV *vs.* NHE observed for the $NiTiO_3$ photoanode, can be credited to the improved photogenerated charge separation in the BiOCl/$NiTiO_3$ heterostructured photoanodes. Additionally, an increase in the slope of BiOCl/$NiTiO_3$ heterostructured photoanodes (5.62×10^9) was obtained (Fig. 2f), as against the 2.48×10^{10} obtained for $NiTiO_3$. Since the slope (obtained from eqn (7)) inversely corresponds to the charge carrier density (equivalent to the electron density), a donor density of 1.79×10^{21} cm^{-3} calculated for BiOCl/$NiTiO_3$ photoanodes is about thrice the donor density obtained for $NiTiO_3$ (4.07×10^{20} cm^{-3}). This further confirms effective and prolonged charge separation at the heterojunction photoanode.

$$E_{fb\,vs.\,NHE} = E_{fb\,vs.\,Ag/AgCl} + 0.194 \quad (pH = 7) \tag{6}$$

$$N_D = \frac{2}{\varepsilon\varepsilon_0 e m} \tag{7}$$

Here, m is the slope obtained from the Mott Schottky plots.

3.4 Photoelectrocatalytic application of the photoanodes for ciprofloxacin degradation

The photoanodes were applied for the photoelectrocatalytic degradation of 5 mg L^{-1} CPX under a 150 W simulated sunlight source with an optimized current density of 5 mA cm^{-2} at pH 7. As presented in Fig. 3a, the heterostructured BiOCl/$NiTiO_3$ photoanode achieved an impressive 94% removal efficiency within 120 min. Its performance surpasses the individual BiOCl and $NiTiO_3$ photoanodes, which achieved 84% and 80% degradation efficiencies, respectively. The improvement in the BiOCl/$NiTiO_3$ heterostructured photoanode performance indicates a significant suppression in the photogenerated charge carrier recombination rate. Hence, the photo-excited heterostructure photoanode exhibits higher mobility than the individual photoanodes, allowing the generated species to attack CPX unselectively. Additionally, photoelectrocatalysis (a combination of photocatalysis and electrocatalysis) demonstrated 94% degradation efficiency compared to 18% and 86% obtained for individual photocatalysis and electrocatalysis techniques (Fig. 3b). The influence of electrochemical driving force (current density) equally facilitated charge separation in the heterostructured photoanode by initiating induced hole injection into the valence band.[40] This effect enriches the availability of generated holes and electrons by drastically extending their lifespan.[46,47] Consequently, the delayed charge recombination aided by enhanced charge migration across the heterostructured photoanode-electrolyte interface can accelerate ROS generation and the simultaneous degradation of the pollutant.

3.5 Kinetic and synergistic studies

The photoelectrocatalytic reaction kinetics were determined for each photoanode (Fig. 3c). Also, photocatalytic and electrocatalytic reaction kinetics for the BiOCl/$NiTiO_3$ heterostructured photoanode were determined and are presented in Fig. 3d. The reaction kinetics of all degradation techniques obtained from the plot of $\ln c_0/c_t$ *versus* time conformed to a pseudo-first-order reaction. The kinetics were fitted into $\ln c_0/c_t = kt$, where c_0, c_t, k, and t are the initial concentration (mg L^{-1}), final concentration (mg L^{-1}), rate constant (min^{-1}), and time (min). Rate constant (k) value of 2.48×10^{-2} min^{-1} ($R^2 = 0.9955$) was obtained for the BiOCl/$NiTiO_3$ heterostructured photoanode, which is approximately 1.55-fold and 1.78-fold of the

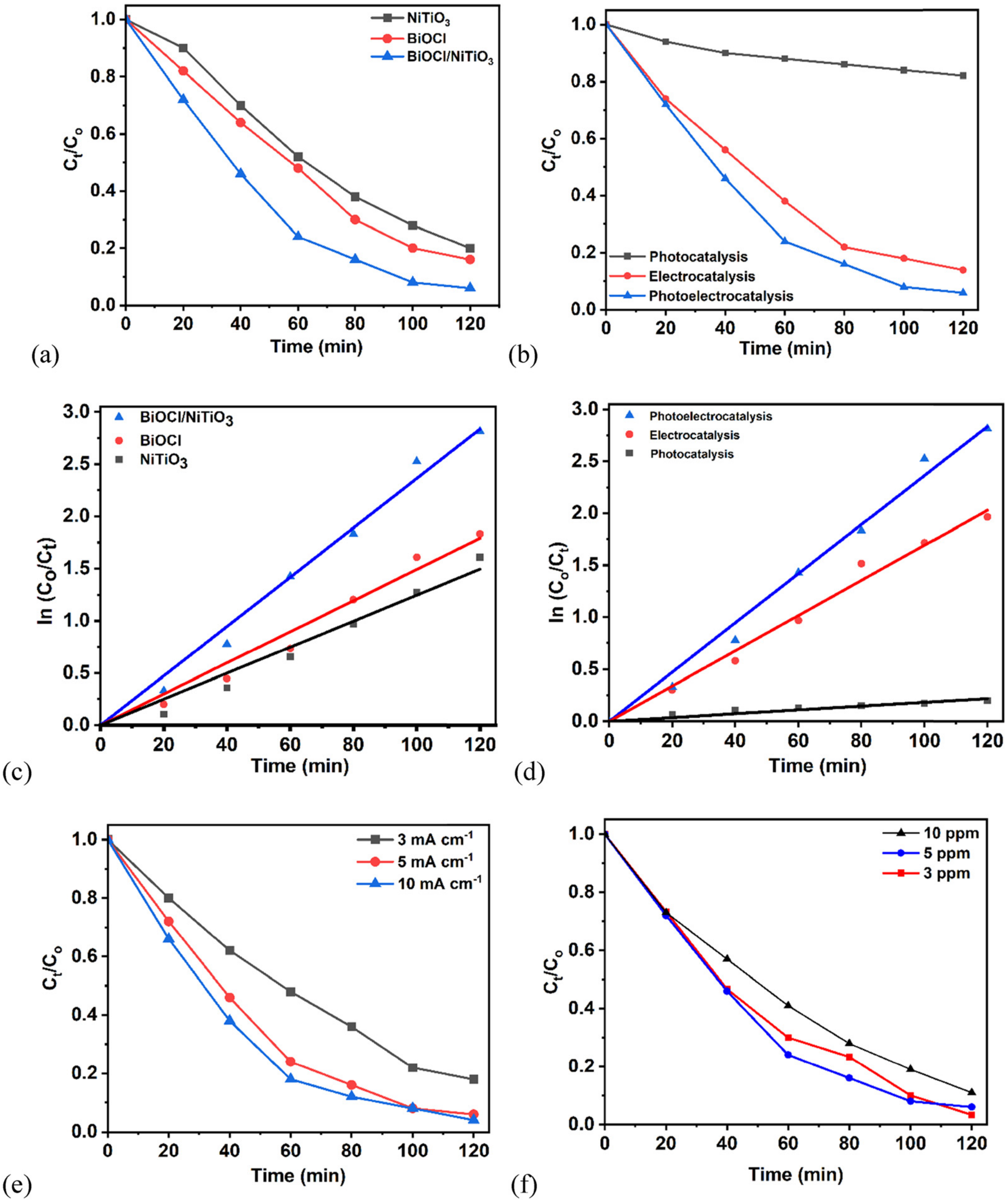

Fig. 3 Degradation efficiency plots of 5 mg L^{-1} CPX (a) on all photoanodes under PEC application, and (b) on the BiOCl/NiTiO$_3$ photoanode, comparing electrocatalysis, photocatalysis and PEC applications. Reaction kinetic plots (c) of all photoanodes under PEC application and (d) on the BiOCl/NiTiO$_3$ photoanode, comparing electrocatalysis, photocatalysis and PEC applications. Plots of PEC degradation efficiencies of CPX on the BiOCl/NiTiO$_3$ photoanode (e) at different current densities and (f) at various initial concentrations of CPX at 5 mA cm^{-2}.

rate constants for BiOCl (1.62×10^{-2} min^{-1}, $R^2 = 0.9894$) and NiTiO$_3$ (1.39×10^{-2} min^{-1}, $R^2 = 0.9869$) photoanodes (Fig. 3c). This outcome agrees with the notable suppression of photogenerated charge carrier recombination in the BiOCl/NiTiO$_3$ photoanode, caused by the improved light absorption capacity of the heterostructure photoanode. Moreover, improved charge mobility in the BiOCl/NiTiO$_3$ heterostructured photoanode eased the generation of reactive oxygen species, thus leading to the impressive degradation of CPX. The photoelectrocatalytic rate constant of the BiOCl/NiTiO$_3$ heterostructured photoanode also showed a 1.66-fold and 13.55-fold increment in the respective electrocatalytic (1.70×10^{-2} min^{-1}, $R^2 = 0.9952$) and photocatalytic (1.83×10^{-3} min^{-1}, $R^2 = 0.9761$) rate constants. The heterostructured photoanode performance during the photoelectrocatalytic degradation of CPX further establishes the desirable synergy arising from combining both electrocatalysis and photocatalysis in the hybrid system.

To further establish the clear advantage of the photoelectrocatalytic technique owing to the influence of the light source and electrochemical driving force (current density), the degree of synergy and electrochemical enhancement (E) were estimated[48] using eqn (8) and (9).

$$\mathrm{SI} = \frac{[k_{\mathrm{PEC}} - (k_{\mathrm{PC}} + k_{\mathrm{E}})]}{k_{\mathrm{PEC}}} \tag{8}$$

$$E = \frac{[k_{\mathrm{PEC}} - k_{\mathrm{PC}}]}{k_{\mathrm{PEC}}} \quad (9)$$

Here, k_{PEC}, k_{PC}, and k_{E} are the rate constants obtained for photoelectrocatalytic, photocatalytic, and electrocatalytic processes. The synergistic index (SI) of 1.612 was estimated. A synergistic index that exceeds zero implies that improvement in the photoelectrocatalytic process emanates from the harmonious alignment between the individual electrocatalytic and photocatalytic processes.[49] Moreover, an estimated 93% electrochemical enhancement was observed during the photoelectrocatalytic degradation of CPX. This implies that the electrochemical driving force has an overwhelming impact on the degradation efficiency of CPX.

3.6 Influence of current density and concentration on the degradation of CPX

The influence of various electrochemical parameters on the degradation efficiency of CPX during photoelectrocatalysis was also evaluated in 0.1 M Na_2SO_4 electrolyte at neutral pH. The degradation efficiency of CPX grew proportionally with increased applied current density. Degradation efficiencies of 82%, 94%, and 96% were obtained upon applying 3 mA cm^{-2}, 5 mA cm^{-2}, and 10 mA cm^{-2} current densities, respectively, as shown in Fig. 3e. This further corroborates the superior influence of current density on the photoelectrocatalytic technique, which arises from improved mass transfer across the $BiOCl/NiTiO_3$ heterostructured photoanode–electrolyte interface. Thus, enhanced migration efficiency of mobile species, including photogenerated charges and ROS, results in a more pronounced charge separation advantage gained by the $BiOCl/NiTiO_3$ photoanode during the process. Additionally, the performance of the $BiOCl/NiTiO_3$ heterostructured photoanode in different concentrations of CPX was evaluated. The degradation efficiencies decreased gradually from 97% to 89% as the initial concentration of CPX increased from 3 mg L^{-1} to 10 mg L^{-1} (Fig. 3f). This pattern may be attributed to the presence of more analytes competing to interact with the reactive oxygen species generated in the system as the initial concentration increases.

3.7 Reusability, stability and scavenger studies

The stability of the $BiOCl/NiTiO_3$ heterostructured photoanode was examined by subjecting it to multiple cycles of photoelectrocatalytic degradation of CPX. The photoanode exhibited remarkable stability at operating conditions involving pH 7 and 5 mA cm^{-2} applied current density. An average degradation efficiency of 92.5% was obtained through five cycles of photoelectrocatalytic degradation of CPX, as shown in Fig. 4a. The stability displayed by the photoanode suggests that a consistent charge separation and interfacial charge migration efficiency occurred each time the photoanode was applied. Moreover, this stability further indicates the viability of the heterostructured photoanode for real-time applications. The structural property of the $BiOCl/NiTiO_3$ heterostructured semiconductor photoanode was examined after its use for multiple cycles of photoelectrocatalytic degradation of CPX. The structural integrity of the heterostructured semiconductor was preserved after photoelectrocatalytic application, as shown in Fig. S3.

The degradation of CPX on the $BiOCl/NiTiO_3$ heterostructured photoanode during photoelectrocatalytic degradation occurred through the influence of reactive oxygen species generated during the process. Due to their high reactivity and low stability, these species attack the bonds of the target organic pollutant non-selectively, resulting in oxidation. In addition to the photogenerated holes and electrons, influential species commonly generated in photoelectrocatalytic systems include hydroxyl radicals and superoxide radicals. Each species was trapped independently using chemical inhibition agents to quench and render them inactive during the photoelectrocatalytic process. Notably, upon inhibiting the activity of $^{\bullet}OH$ in the system with terephthalic acid, the degradation efficiency declined by 15% (Fig. 4b), showing that $^{\bullet}OH$ was the most predominant ROS responsible for the degradation of CPX. A 27% reduction in the degradation efficiency upon trapping h^+_{VB} with EDTA suggests that the photogenerated hole also played a significant role in the degradation process. However, drastic contractions in the degradation efficiency were obtained upon inhibiting $O_2^{\bullet -}$ and e^-_{CB} to 21% and 36%, respectively, indicative of a limited influence of these species in the degradation of CPX. Eqn (10)–(14) show possible formation routes for the species in the photoelectrocatalytic system.

$$\begin{aligned} &BiOCl/NiTiO_3 \text{ heterostructured photoanode} + h\nu \\ &\quad \rightarrow BiOCl/NiTiO_3\ (h^+_{VB}, e^-_{CB}) \end{aligned} \quad (10)$$

$$h^+_{VB} + H_2O \rightarrow {}^{\bullet}OH + H^+ \quad (11)$$

$$h^+_{VB} + OH^- \rightarrow {}^{\bullet}OH \quad (12)$$

$$e^-_{CB} + O_2 \rightarrow O_2^{\bullet -} \quad (13)$$

$$({}^{\bullet}OH, O_2^{\bullet -}, h^+) + \text{ciprofloxacin} \rightarrow CO_2 + H_2O \quad (14)$$

3.8 Proposed Z-scheme mechanism of the heterostructured photoanode

The proposed scheme illustrated in Fig. 4c shows that the $BiOCl/NiTiO_3$ heterostructured photoanode exhibits type II behaviour. Photogenerated holes and electrons are produced in the semiconductors upon irradiation, resulting in the formation of valence and conduction bands within their interfacial structure, as illustrated by eqn (9). Before contact between the pristine semiconductors was initiated, the conduction band and valence band of $NiTiO_3$ partially overlapped with the energy band edges of BiOCl, as obtained from the calculations of UV-vis DRS and Mott Schottky plots. Following contact initiation, Fermi level alignment is achieved within the heterostructure photoanode, resulting in a staggered alignment. Generally, heterostructure mechanisms and formation between interacting semiconductors are influenced by band bending or internal electric fields created at the interface of the participating semiconductors. Other influencing parameters include the position of their conduction and valence band edges, the semiconductor type, Fermi energy levels, and work

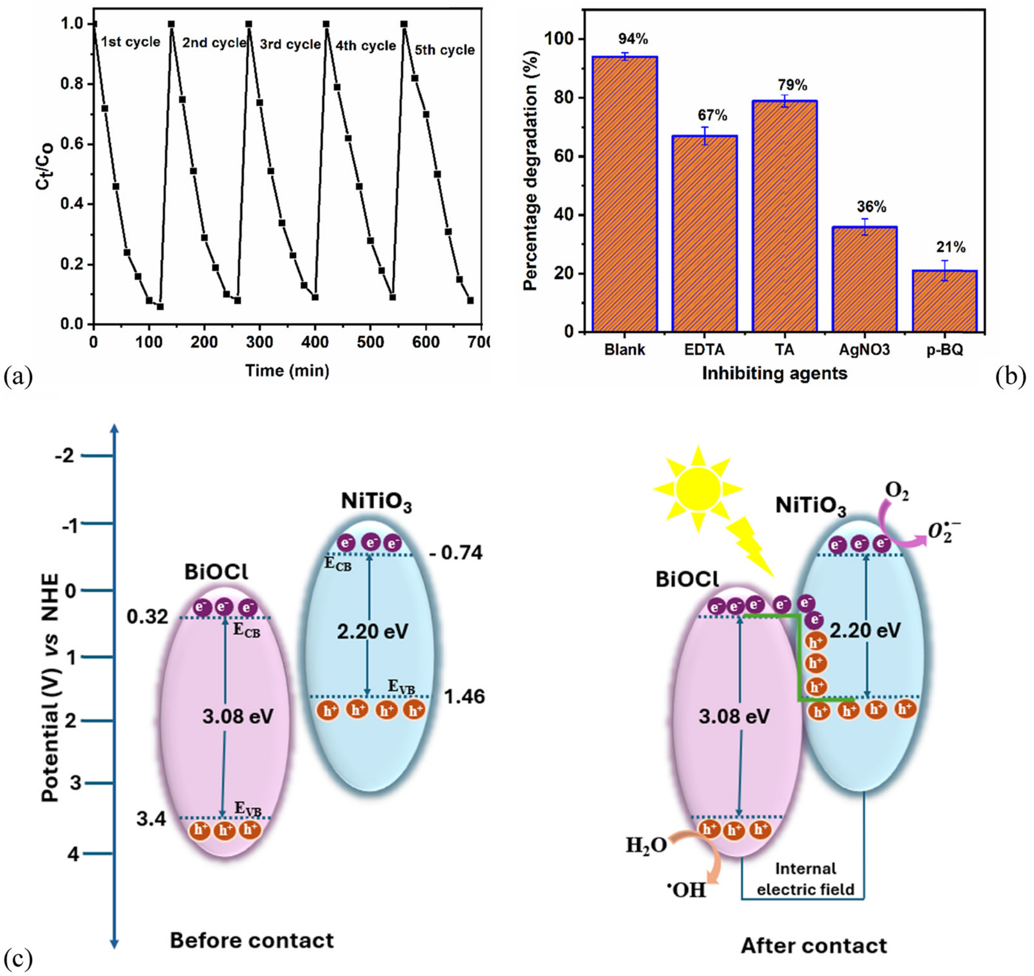

Fig. 4 (a) Reusability plot of the BiOCl/NiTiO$_3$ heterostructured photoanode for 5 mg L^{-1} CPX degradation under PEC application, (b) scavenger studies of ROS in the PEC system on the BiOCl/NiTiO$_3$ heterostructured photoanode, and (c) Z-scheme behaviour of the BiOCl/NiTiO$_3$ heterostructured photoanode.

function.[14] Typical of a type II (Z-scheme) alignment, the electron from the conduction band of BiOCl recombines with the holes in the valence band of NiTiO$_3$ upon irradiation through interfacial transmission.[50,51] This spontaneous transmission leads to the formation of an internal electric field at the interface of the heterostructured photoanode, which is often observed in p–n heterostructure behavior.[52] The induced internal electric field gives rise to an upward band bending and electron depletion (hole accumulation) in NiTiO$_3$, while a downward band bending and electron accumulation in BiOCl is initiated. This results in attraction between the positively charged valence band of NiTiO$_3$ and the negatively charged conduction band of BiOCl at the heterostructured photoanode interface, allowing electrons to migrate from the conduction band of BiOCl to the valence band of NiTiO$_3$. Since the Fermi level of BiOCl (0.37 eV) is more positive than that of NiTiO$_3$ (−0.36 eV), the proposed mechanism agrees with Z-scheme behaviour, which allows electron migration from the semiconductor with a higher Fermi level to the semiconductor with a lower Fermi level.[53]

Similarly, the internal electric field formed within the BiOCl/NiTiO$_3$ interface promoted spontaneous interfacial electron diffusion from BiOCl due to its lower work function (W_f) (range of 5.19–5.56 eV *vs.* NHE, pH = 7[54,55]) to NiTiO$_3$ with a higher work function (W_f = 5.86 eV *vs.* NHE, pH = 7[56]). This migration path is triggered by the ease of electron mobility from the core to the surface of a semiconductor with a lower work function in a heterostructured semiconductor.[55] Consequently, available holes at the valence band of BiOCl readily react with water to form hydroxyl radicals ($^{\bullet}$OH), and separated electrons at the conduction band of NiTiO$_3$ react with dissolved oxygen in the system to form superoxide radicals ($O_2^{\bullet-}$) as represented in eqn (10) and (11). The formation of $O_2^{\bullet-}$ is stimulated by the more negative potential (−0.74 eV) attainable at the conduction band of NiTiO$_3$ than $O_2/O_2^{\bullet-}$ = −0.33 V *vs.* NHE standard potential, while $^{\bullet}$OH formation is encouraged by a more positive potential (3.4 eV) reached by the valence band of BiOCl than the standard potential of H_2O/O_2 = 2.37 V *vs.* NHE. Additionally, the significant charge separation modelled by the BiOCl/NiTiO$_3$ heterostructured photoanode agrees with its transient photocurrent response, which is twice the responses obtained for individual semiconductors. This accelerated photogenerated charge separation and reduced recombination arising from charge redistribution eases reactive oxygen species generation, while improving charge mobility. Consequently, the oxidation process involving the breaking of the organic bond in CPX to non-toxic H_2O and CO_2 occurs at the photoanode surface.

4. Conclusion

The BiOCl/$NiTiO_3$ heterostructured semiconductor and its photoanode were successfully fabricated and applied for the photoelectrocatalytic degradation of ciprofloxacin in water. The synergistic integration gained from combining BiOCl and $NiTiO_3$ semiconductors yielded a superior heterostructured photoanode with improved charge separation and mobility. The results from the electrochemical, optical, and photoelectrocatalytic characterization of the semiconductors showed that superior charge transfer and reduced charge recombination are easily attainable in BiOCl/$NiTiO_3$ compared with the individual semiconductors. Moreover, the BiOCl/$NiTiO_3$ heterostructured photoanode achieved more impressive efficiency than the individual BiOCl/$NiTiO_3$ photoanodes when applied for the photocatalytic degradation of 5 mg L^{-1} of CPX. The overall photoelectrocatalytic degradation was generally performed by maintaining operating conditions of 5 mA cm^{-1} current density, 50 mL working solution containing 0.1 M Na_2SO_4 supporting electrolyte at neutral pH, and a 150 W lamp. The proposed reaction mechanism deduced from optical properties revealed that the BiOCl/$NiTiO_3$ heterostructured photoanode exhibits Z-scheme behaviour. The calculated valence band of BiOCl exceeding the standard oxidation potential required for water oxidation (H_2O/O_2 = 2.37 V *vs.* NHE) explains the significance of h^+ during CPX degradation and the ease of hydroxyl radical generation in the system. These findings underscore the importance of rational heterostructured photoanode designs in advancing photoelectrocatalytic technologies in wastewater remediation.

Conflicts of interest

There are no conflicts of interest to declare.

Data availability

The data supporting this article have been included as part of the supplementary information (SI). The supplementary information includes the EDX spectra of BiOCl/$NiTiO_3$ heterostructured semiconductor, Mott Schottky plot of BiOCl and $NiTiO_3$ photoanodes and the XRD pattern of the BiOCl/$NiTiO_3$ heterostructured semiconductor before and after use. See DOI: **https://doi.org/10.1039/d5ma00827a**.

Acknowledgements

Financial support from the Centre of Nanomaterial Science Research, University of Johannesburg (grant no. 086342) and Global Excellence Scholarship, University of Johannesburg (grant no. 105592), is greatly appreciated.

References

1 R. Wu, Y. Ruan, H. Lin, C. N. T. Yuen, H. Feng and P. K. S. Lam, *ACS EST Water.*, 2021, **1**, 542–552.
2 A. B. de Souza, N. Gadi, T. van de Goor, N. C. Boelee, R. Dewil and D. Cabooter, *J. Water Process Eng.*, 2024, **66**, 105899.
3 O. F. S. Khasawneh and P. Palaniandy, *Process Saf. Environ. Prot.*, 2021, **150**, 532–556.
4 M. Hossein and A. S. Ripanda, *Toxicol. Rep.*, 2025, **14**, 101969.
5 M. Kukreja, A. A. Kumar, N. Haq and K. A. Siddiqui, *Mater. Today Commun.*, 2025, **45**, 112403.
6 M. C. Danner, A. Robertson, V. Behrends and J. Reiss, *Sci. Total Environ.*, 2019, **664**, 793–804.
7 B. Böger, M. Surek, R. D. O. Vilhena, M. M. Fachi, A. M. Junkert, J. M. Santos, E. L. Domingos, A. D. F. Cobre, D. R. Momade and R. Pontarolo, *J. Hazard. Mater.*, 2021, **402**, 123448.
8 M. Kang, J. Yang, S. Kim, J. Park, M. Kim and W. Park, *Sci. Total Environ.*, 2022, **811**, 152331.
9 C. F. Couto, L. C. Lange and M. C. S. Amaral, *J. Water Process Eng.*, 2019, **32**, 100927.
10 A. Pietro, S. Murgolo, C. De Ceglie, G. Mascolo, M. Carmagnani, P. Ronco, M. Bestetti and S. Franz, *Catal. Today*, 2025, **450**, 115205.
11 X. Meng and Z. Zhang, *Catal. Today*, 2018, **315**, 2–8.
12 D. Kanakaraju, B. D. Glass and M. Oelgemöller, *J. Environ. Manage.*, 2018, **219**, 189–207.
13 L. Shi, Y. Yin, L. C. Zhang, S. Wang, M. Sillanpää and H. Sun, *Appl. Catal., B*, 2019, **248**, 405–422.
14 A. Balapure, J. Ray Dutta and R. Ganesan, *RSC Appl. Interfaces*, 2024, **1**, 43–69.
15 Z. Li, Y. Qu, K. Hu, M. Humayun, S. Chen and L. Jing, *Appl. Catal., B*, 2017, **203**, 355–362.
16 Z. Jia, R. Lv, L. Guo, J. Zhang, R. Li, J. Liu and C. Fan, *Sep. Purif. Technol.*, 2021, **257**, 117872.
17 X. Zhou, J. Liu and J. Sun, *Adv. Compos. Hybrid Mater.*, 2024, **7**, 239.
18 L. Li, G. Liu, J. Dong, S. Cao, B. Wang, J. Zhao, M. Ji, Y. She, J. Xia and H. Li, *Appl. Surf. Sci.*, 2025, **697**, 162978.
19 Z. Xu, C. Zhang, Y. Zhang, Y. Gu and Y. An, *Inorg. Chem. Commun.*, 2022, **138**, 109277.
20 D. Sun, M. Zhang, L. Huang, Y. Qu, Y. Yu, B. Lou, H. Du, B. Xu and K. Wang, *J. Alloys Compd.*, 2023, **969**, 172433.
21 D. Peng, Y. Wang, H. Shi, W. Jiang, T. Jin, Z. Jin and Z. Chen, *J. Colloid Interface Sci.*, 2022, **613**, 194–206.
22 S. Li, S. Hu, W. Jiang, Y. Liu, Y. Zhou, Y. Liu and L. Mo, *J. Colloid Interface Sci.*, 2018, **521**, 42–49.

23 B. O. Ojo, O. A. Arotiba and N. Mabuba, *Colloids Surf., A*, 2022, **647**, 129201.

24 T. Yao, X. An, H. Han, J. Q. Chen and C. Li, *Adv. Energy Mater.*, 2018, **8**, 1–36.

25 A. Vilanova, P. Dias, T. Lopes and A. Mendes, *Chem. Soc. Rev.*, 2024, **53**, 2388–2434.

26 E. Brillas, *Chemosphere*, 2020, **250**, 126198.

27 Z. Zhang, Y. Yuan, L. Liang, Y. Fang, Y. Cheng, H. Ding, G. Shi and L. Jin, *Ultrason. Sonochem.*, 2008, **15**, 370–375.

28 S. Fekadu, E. Alemayehu, R. Dewil and B. Van der Bruggen, *J. Appl. Electrochem.*, 2021, **51**, 607–618.

29 S. Fekadu, E. Alemayehu, B. Oljira, S. Tiku, D. Dadi and B. Van der Bruggen, *J. Water Process Eng.*, 2021, **41**, 102068.

30 S. Fekadu, E. Alemayehu, P. Asaithambi and B. Van der Bruggen, *Int. J. Environ. Res.*, 2022, **16**, 1–11.

31 M. Chettab, Q. Simon, M. Zaghrioui, C. Autret-Lambert and P. Laffez, *Thin Solid Films*, 2020, **714**, 138384.

32 J. Wang, Y. Wei, B. Yang, B. Wang, J. Chen and H. Jing, *J. Catal.*, 2019, **377**, 209–217.

33 A. Hao, X. Ning, X. Liu, L. Zhan and X. Qiu, *Chem. Eng. J.*, 2024, **499**, 155823.

34 W. Li, S. Ao He, Z. Ying Su, W. Xu and X. Chuan Wang, *Appl. Surf. Sci.*, 2019, **470**, 707–715.

35 J. Bai, X. Zhang, C. Wang, X. Li, S. Cao, R. Zhang, X. Xiao, X. Jiang and T. Wu, *Sep. Purif. Technol.*, 2025, **361**, 131521.

36 S. Dhingra, M. Sharma, V. Krishnan and C. M. Nagaraja, *J. Colloid Interface Sci.*, 2022, **615**, 346–356.

37 D. Peng, L. Mao, J. Sun, X. Li, H. Shi and Z. Su, *Int. J. Hydrogen Energy*, 2025, **114**, 60–70.

38 X. Ren, J. Yao, L. Cai, J. Li, X. Cao, Y. Zhang, B. Wang and Y. Wei, *New J. Chem.*, 2019, **43**, 1523–1530.

39 S. Sharma, A. D. Acharya, Y. S. Thakur and Bhawna, *Mater. Res. Bull.*, 2025, **183**, 113214.

40 K. D. Jayeola, D. S. Sipuka, T. I. Sebokolodi, J. O. Babalola, M. Zhou, F. Marsken and O. A. Arotiba, *ACS Appl. Mater. Interfaces*, 2025, **17**, 1385–1398.

41 B. O. Ojo, O. A. Arotiba and N. Mabuba, *J. Environ. Chem. Eng.*, 2022, **10**, 107224.

42 S. M. Tan and M. Pumera, *ACS Nano*, 2019, **13**, 2681–2728.

43 Q. Wang, L. Ren, J. Zhang, X. Chen, C. Chen, F. Zhang, S. Wang, J. Chen and J. Wei, *Adv. Energy Mater.*, 2023, **13**, 2301543.

44 B. O. Orimolade and O. A. Arotiba, *Sci. Rep.*, 2020, 1–13.

45 K. Sivula, *ACS Energy Lett.*, 2021, **6**, 2549–2551.

46 J. P. Velasquez-Tamayo, D. A. Torres-Ceron, S. Amaya-Roncancio, S. I. Santacruz, C. D. Acosta-Medina and E. Restrepo-Parra, *Chem. Eng. J.*, 2023, **477**, 147080.

47 X. Yang and D. Wang, *ACS Appl. Energy Mater.*, 2018, **1**, 6657–6693.

48 B. O. Orimolade, B. N. Zwane, B. A. Koiki, L. Tshwenya, G. M. Peleyeju, N. Mabuba, M. Zhou and O. A. Arotiba, *J. Environ. Chem. Eng.*, 2020, **8**, 103607.

49 A. Amedlous, M. Majdoub, E. Amaterz, Z. Anfar and A. Benlhachemi, *J. Photochem. Photobiol., A*, 2021, **409**, 113127.

50 D. Huang, X. Yan, M. Yan, G. Zeng, C. Zhou, J. Wan, M. Cheng and W. Xue, *ACS Appl. Mater. Interfaces*, 2018, **10**, 21035–21055.

51 Y. Wang, Z. Ma, J. Wang, J. Ben, H. Guan, P. Gu and Y. Hu, *Mater. Sci. Semicond. Process.*, 2025, **190**, 109375.

52 J. Low, J. Yu, M. Jaroniec, S. Wageh and A. A. Al-Ghamdi, *Adv. Mater.*, 2017, **29**, 1601694.

53 T. Di, Q. Xu, W. K. Ho, H. Tang, Q. Xiang and J. Yu, *ChemCatChem*, 2019, **11**, 1394–1411.

54 S. Gong, F. Rao, W. Zhang, Q. U. Hassan, Z. Liu, J. Gao, J. Lu, M. Hojamberdiev and G. Zhu, *Chin. Chem. Lett.*, 2022, **33**, 4385–4388.

55 L. Zhao, H. Hou, S. Wang, L. Wang, Y. Yang, C. R. Bowen, J. Wang, Z. Liao, D. Yang, R. Yan and W. Yang, *Adv. Funct. Mater.*, 2024, **2416346**, 1–16.

56 B. Li, W. Wang, J. Zhao, Z. Wang, B. Su, Y. Hou, Z. Ding, W. J. Ong and S. Wang, *J. Mater. Chem. A*, 2021, **9**, 10270–10276.